Colloidal Hard-Sphere Crystal Growth Frustrated by Large Spherical Impurities

Volkert W. A. de Villeneuve, Roel P. A. Dullens, Dirk G. A. L. Aarts, Esther Groeneveld, Johannes H. Scherff, Willem K. Kegel, Henk N. W. Lekkerkerker*

Impurities affect the nucleation, growth, and structure of crystals. Here we report the effect of large, spherical, polymethylmethacrylate impurities on the crystal growth of monodisperse, hard, polymethylmethacrylate colloids in a density- and optically matching apolar solvent mixture. Crystal growth, initiated at the bottom of the sample, was studied by imaging sequences of two-dimensional *xy* slices in the plane of the impurity's center with a laser scanning confocal microscope. Impurities form the center of grain boundaries, and a single fluid particle layer around the impurity persists in all cases. The growth rate sensitively depends on the impurity's size. Crystal growth is inhibited to a greater extent near smaller impurities, pointing to local crystal frustration induced by the curvature of the impurity.

Impurities substantially affect crystal nucleation and growth, whether present as an unavoidable nuisance or intentionally added to modify a product or process. Depending on the nature of both the impurity and the main component(s), nucleation and crystal growth are either inhibited, suppressed, or promoted (*1*–*5*). Great effort has been put into understanding many of these altered processes, which are crucial to areas as diverse as the pharmaceutical industry (*6*), mineralogy (*7*), semiconductors (*8*), single-crystal production (*1*, *2*), polymer processing (*9*), and protein crystals (*10*).

We consider the introduction of a large hard sphere, which is the simplest conceivable impurity, into a growing crystal of hard spherical particles. The particle sizes and time scales in colloidal systems enable real-time studies down to the particle level and are therefore excellent model systems for such studies. The impurity (i)/particle (p) diameter ratio $\alpha \equiv (\sigma_i/\sigma_p)$ is a critical factor for such systems: In two-dimensional (2D) binary arrays, translational order is substantially reduced (*11*) and crystal nucleation can be inhibited in polydisperse 3D systems (*12*). In contrast, a single impurity in a metastable fluid phase may induce crystallization by heterogeneous nucleation (*3*). A sphere with infinite diameter (that is, a flat wall) can induce a pre-freezing transition (*13*, *14*). We studied the influence of impurity curvature on a crystal growing around impurities with ratios of α = 5 to 21, which is a different scenario than a crystal nucleating on a curved surface (*3*).

We obtained very large, polydisperse, fluorescently labeled polymethylmethacrylate spheres (PMMA) with diameters ranging from 100 nm to 100 μm from a synthesis following the method of (*15*). A small amount (<0.1 weight %) of these particles, size-fractionated by sedimentation, was mixed with 6% polydisperse 1.5-μm-diameter PMMA particles in an apolar solvent mixture of tetraline, cis-decaline, and tetrachloromethane (solvent volume fractions = 0.35/0.30/0.35; density difference $\Delta\rho \approx$ 0.01 g/ml; and refractive index mismatch $\Delta n_D \approx$ 0.005) (*16*), with a 5-mm sample height. At a 0.55 volume fraction, the high viscosity minimizes impurity diffusion. The crystal nucleates heterogeneously at the glass sample bottom and grows upward, as shown by a control experiment without impurities (Fig. 1A and supporting online material). Homogeneous nucleation occurs only far from the wall. The impurity locks into its current position and moves less than the colloidal particle diameter over several hours. In a sense, this is the reverse scenario from (*17*), where a crystal is disturbed by an external pressure after it has formed. Sequences of 2D *xy* slices were imaged in the plane of the impurity's center; near impurities with α = 5, 10, ~13, and ~ 21 (referred to as I_5, I_{10}, I_{13}, and I_{21}, respectively); 15 to 25 μm above the glass sample bottom; at a rate of three to six slices per minute; up to 2 hours after homogenization. Imaging was performed with a Nikon Eclipse TE2000U confocal microscope with a Nikon C1 scanning head.

Representative confocal slices of crystal growth near impurities are shown in Fig. 1, B to E. Around impurity I_5, crystal growth is initially observed only far from the impurity (Fig. 1B1). The crystal front subsequently grows toward the impurity but is clearly frustrated (Fig. 1B). Frustration is characterized both by limited growth near the impurity (dynamic frustration) and by persistant grain boundaries directed toward the impurity (static frustration). In Fig. 1, C and D, frustration near I_{10} and I_{13} is reduced: A crystal front is present, but crystal growth is observed near the impurity's shell as well (Fig. 1, C2 and D1). Particles in the first layer around the impurity do not crystallize at all; particles in the second layer crystallize only very slowly (Fig. 1, C2 and D2). Here, a relatively low degree of crystallinity during late stages of crystal growth is observed (Fig. 1, C3 and D3). Finally, crystal growth near I_{21} occurs all through the field of view (Fig. 1E). Particles neighboring the impurity are far more dynamic than bulk particles and appear fluidlike (Fig. 1E). Other impurities appear in the field of view through diffusion and sedimentation for this particular sequence. These clearly affect crystal growth, as observed from the grain boundaries connecting impurities. This is not apparent in all cases, because some impurities lie outside the field of view. Grain size seems to scale with impurity size, but the limited data set prohibits statistical analysis. The control experiment also reveals that samples with and without impurities initially have a comparable number of grain boundaries (Fig. 1, A to E, and fig. S1). At low impurity concentrations, the impurities therefore pin the grain boundaries but do not increase their quantity. The grain boundaries gradually anneal in a sample without impurities (Fig. 2C and fig. S3), but persist in between impurities (Fig. 2A).

Several trends are obtained from mere visual comparison of the slice sequences for different values of α. Crystal growth in the first few layers around the impurity seems to proceed faster as α increases. In all sequences, the grain boundaries are directed toward the impurities. The grain boundaries are a consequence of both simultaneous crystal growth at different locations and structural frustration caused by the impurity (Fig. 2, A and B). The first layer around the impurity fails to crystallize: 18 hours after homogenization the fluidlike character of the first layer is still observed (Fig. 2D). At different volume fractions, the same scenario occurs; although at lower volume fractions, sedimentation of the impurity makes experiments difficult. At higher volume fractions, a transition to a glassy state occurs.

To quantify the impurity's effect on local crystal growth, we use the local orientational bond order parameter ψ_6 (*18*)

$$\psi_6(\vec{r}) = \frac{1}{N}\sum_j^N e^{6i\theta(\vec{r_j})} \qquad (1)$$

where $\psi_6 = 1$ for a perfect 2D hexagonal crystal. The summation j runs over all N next neighbors of a given particle. The angle between the bond vector connecting the particle with next neighbor j and an arbitrary fixed reference axis is defined as $\theta(\vec{r_j})$. Particle coordinates are obtained by methods such as those in (*19*). The minimal translation and rotation of the impu-

Van't Hoff Laboratory, Debye Research Institute, University of Utrecht, Padualaan 8, 3584 CH Utrecht, Netherlands.

*To whom correspondence should be addressed. E-mail: h.n.w.lekkerkerker@chem.uu.nl

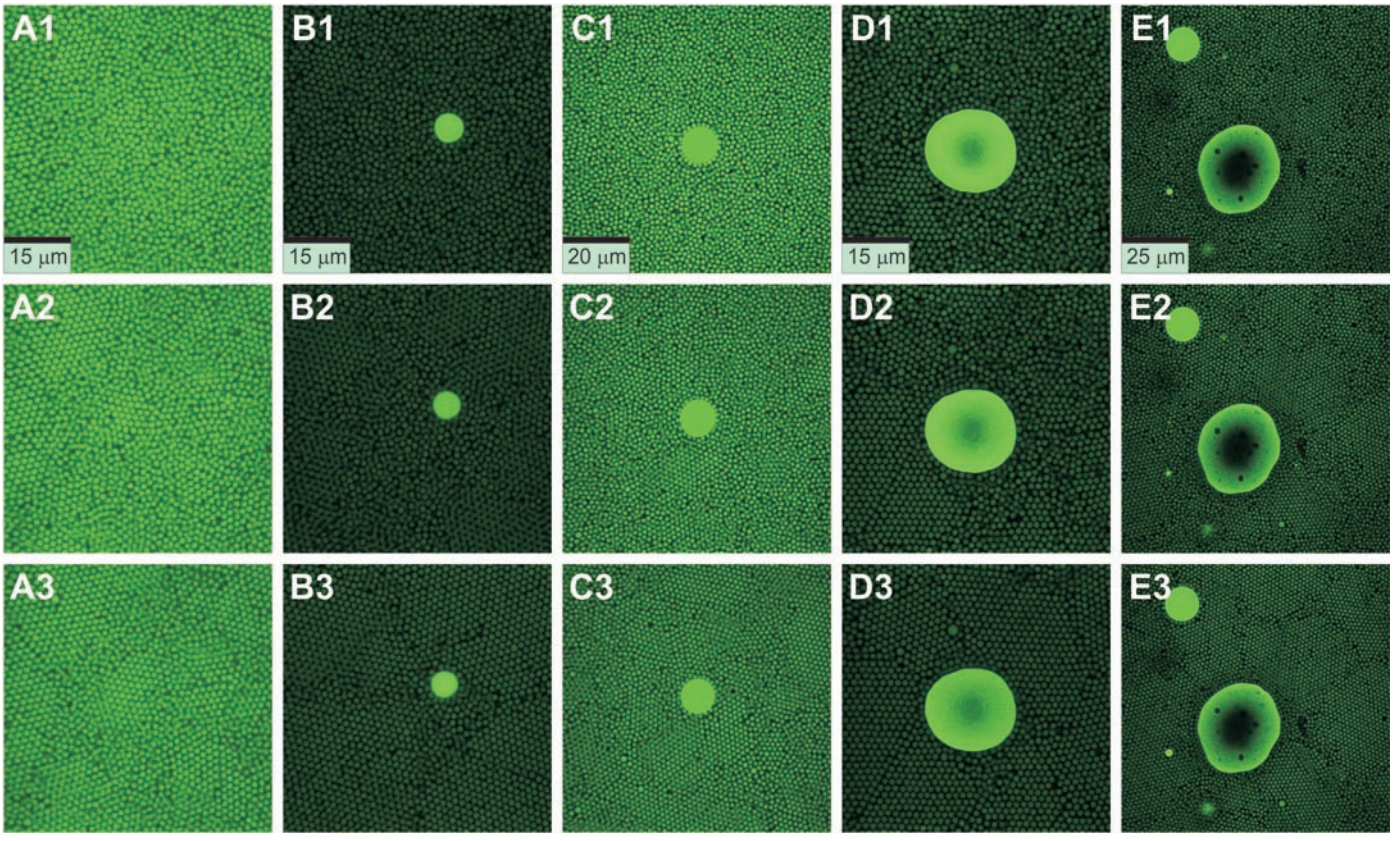

Fig. 1. Confocal images of crystal growth in a sample without impurities (**A**) and near spherical impurities (**B** to **E**). (A) 22 μm above the sample bottom at (A1) 40 min, (A2) 48 min, and (A3) 55 min. (B) I_5 at (B1) 31 min, (B2) 50 min, and (B3) 90 min. (C) I_{10} at (C1) 68 min, (C2) 86 min, and (C3) 103 min. (D) I_{13} at (D1) 41 min, (D2) 57 min, and (D3) 82 min. (E) I_{21} at (E1) 74 min, (E2) 82 min, and (E3) 94 min. Times are the times after sample homogenization.

rity are tracked as well. Particles are divided in shells around the impurity, based on the distance to its shell. Averaging over all particles of shell s, its hexagonal order parameter $\langle|\psi_6|\rangle_s$ is obtained, which is used to obtain a time-dependent crystal growth profile per shell. The presence of other impurities in the I_{21} sequence was "filtered out" (Fig. 3A).

Typical crystal growth profiles of shells 5.0 μm thick around I_{10} are shown in Fig. 3B. All shells start crystallizing simultaneously. The shells evolve from a fluid $\langle|\psi_6|\rangle_s \approx 0.4$ into a more crystalline $\langle|\psi_6|\rangle_s \approx 0.8$, where $\langle|\psi_6|\rangle_s$ reaches a plateau. A constant $\langle|\psi_6|\rangle_s$ value is not reached for the first shell during the image sequence. Crystal growth clearly takes place more rapidly further away from the impurity. An inner shell will have a larger proportion of its shell made up of grain boundaries than will an outer shell. This contributes to the lower observed growth rate close to the impurity. Similar initial and final $\langle|\psi_6|\rangle_s$ values are observed for all α. The degree of crystallinity rises faster with distance to the impurity as α increases, however. This is nicely illustrated in Fig. 3C for the 15- to 20-μm shell, where t_0 indicates the time at which $\langle|\psi_6|\rangle_s$ starts steadily increasing. Crystal growth sets in before I_5 has been locked at its position at depths above ~10 layers. The impurity slowly moves downward because of gravity, which limits the sequences to relatively short intervals, and these are therefore not shown.

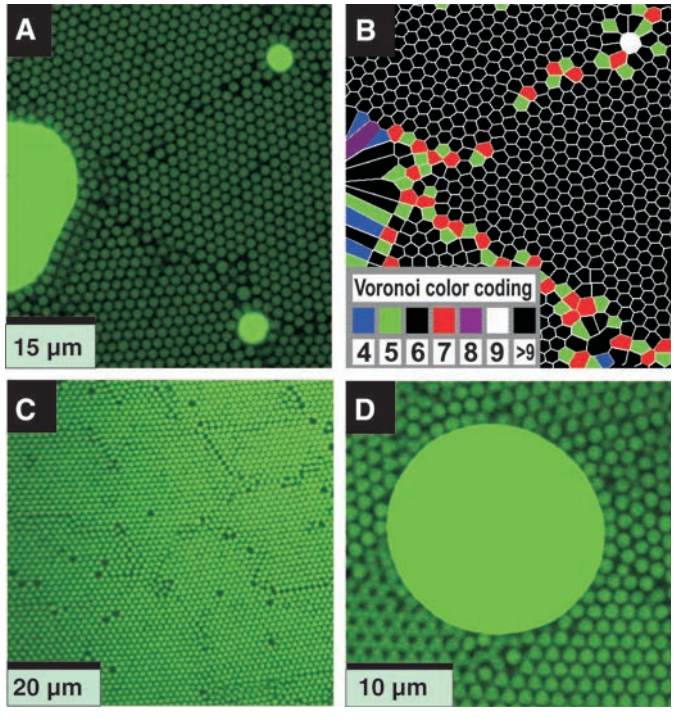

Fig. 2. Grain boundaries and the persisting fluid layer. (**A**) Grain boundaries connect impurities [height, 10 μm; time (*t*), 17 hours]. (**B**) Voronoi representation of (A). Voronoi polygon centers are particle positions. The number of vertices equals the number of next neighbors graphically represented by the color coding in the image. The defects nicely depict the grain boundary. (**C**) In a sample without impurities, grain boundaries have annealed (height, 20 μm; *t*, 13.5 hours). (**D**) The mobile layer of single-particle thickness around an impurity with diameter ratio $\alpha = 13$ appears fluidlike (height, 38 μm; *t*, 18 hours). Heights are distances to the sample bottom. Times are the times after sample homogenization.

The increase in $\langle|\psi_6|\rangle_s$ is approximately linear right after the initial rise. We use this to define the 2D growth rate r_C of shell s

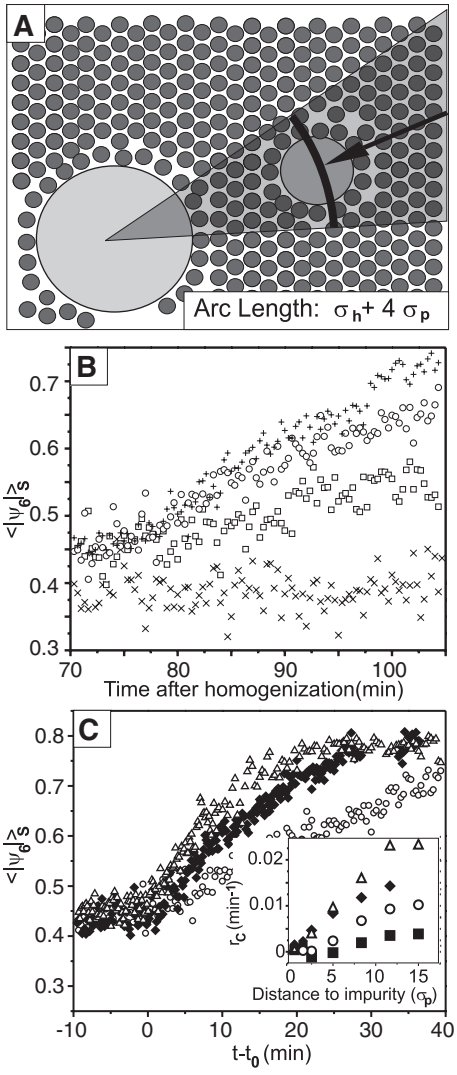

Fig. 3. Quantitative analysis of crystal growth. (**A**) Filtering: Areas affected by other impurities (with a diamenter σ_h) are not taken into account by excluding the shaded area for analysis. (**B**) Crystal growth profiles of shells around I_{10}: 0 to 5 μm (crosses), 5 to 10 μm (squares), 10 to 15 μm (circles), and 15 to 20 μm (plus signs). (**C**) Crystal growth profile of the 15- to 20-μm shell for I_5 (squares, inset only), I_{10} (circles), I_{13} (diamonds), and I_{20} (triangles). (Inset) Frustration of crystal growth increases both as the impurity is approached and as α is decreased. r_C close to I_5 is ~0, because no local increase of order occurs during the recorded image sequence. Rates at 0.5, 1.5, and 2.5 σ_p are based on shells of σ_p thickness. Other r_C values are obtained from shells 5 μm thick: r_C at 5 σ_p corresponds to the 5- to 10-μm shell.

(during linear rise) as $r_C = \Delta\langle|\psi_6|\rangle_s/\Delta t$. The effect of an impurity's size on the local growth rate can now be compared quantitatively (Fig. 3C, inset). Several general trends can be observed. First, a larger α results in a higher rate close to the impurity. Second, the rate rises faster per shell as α increases. Finally, the rates for different α apparently approach a different maximum rate at less than ~17 particle diameters instead of converging to a bulk growth rate of ~0.02 min^{-1} [measured at 5 to 25 μm above the sample bottom in the control sample (fig. S2) and at sample locations far (>40 μm) from impurities]. Relatively far from the impurity (>8 σ_p), a trend is observed between the growth rate and α. We argue that grain boundaries are pinned by impurities (Fig. 2, A and B): If nearby impurities are present, more boundaries appear. To approximate the ideal case of no nearby impurities, the image is filtered (Fig. 3A); grain boundaries leading to impurities further away are not included. The obtained increase of r_C by a factor of 1.6 for the filtered I_{21} sequence therefore is too high, whereas not filtering leads to values that are too low. We therefore expect the rates to converge at sufficient distance, which might very well be beyond ~17 particle diameters. Furthermore, the growth rate in the first layer is about zero for all α—a confirmation of the observed fluid layer (Fig. 2D).

Using laser confocal scanning microscopy, we have shown that the bulk crystal growth rate is substantially reduced near impurities. The extent to which the growth rate is reduced decreases with distance to the impurity. The size ratio α is a critical factor; the (local) curvature of an impurity is therefore crucial for real hard-sphere–like systems such as metals. Grain boundaries are pinned by the impurities, and the first particle layer around the impurity remains fluid. Impurities locally substantially frustrate the crystal growth and structure of hard-sphere systems, the very same impurities that, in a different scenario, can induce heterogeneous crystal nucleation (*3*).

References and Notes

1. N. Kubota, *Cryst. Res. Technol.* **36**, 749 (2001).
2. T. A. Land, T. L. Martin, S. Potapenko, G. T. Palmore, J. J. De Yoreo, *Nature* **399**, 442 (1999).
3. A. Cacciuto, S. Auer, D. Frenkel, *Nature* **428**, 404 (2004).
4. T. A. Eremina *et al.*, *J. Cryst. Growth* **273**, 586 (2005).
5. M. Rak *et al.*, *J. Cryst. Growth* **273**, 577 (2005).
6. A. J. Malkin, Y. G. Kuznetsov, T. A. Land, J. J. Deyoreo, A. McPherson, *Nat. Struct. Biol.* **2**, 956 (1995).
7. K. J. Davis, P. M. Dove, J. J. De Yoreo, *Science* **290**, 1134 (2000).
8. D. T. J. Hurle, P. Rudolph, *J. Cryst. Growth* **264**, 550 (2004).
9. R. Kern, R. Dassonville, *J. Cryst. Growth* **116**, 191 (1992).
10. S. D. Durbin, G. Feher, *Annu. Rev. Phys. Chem.* **47**, 171 (1996).
11. D. Nelson, M. Rubinstein, F. Spaepen, *Philos. Mag. A* **46**, 105 (1982).
12. S. Auer, D. Frenkel, *Nature* **413**, 711 (2001).
13. M. Dijkstra, *Phys. Rev. Lett.* **93**, 103303 (2004).
14. S. Auer, D. Frenkel, *Phys. Rev. Lett.* **91**, 015703 (2003).
15. G. Bosma *et al.*, *J. Colloid Interface Sci.* **245**, 292 (2002).
16. E. H. A. de Hoog, thesis, University of Utrecht, Utrecht, the Netherlands (2001).
17. P. Schall, I. Cohen, D. A. Weitz, F. Spaepen, *Science* **305**, 1944 (2004).
18. D. Nelson, *Defects and Geometry in Condensed Matter Physics* (Cambridge Univ. Press, Cambridge, 2002), pp. 68–91.
19. J. C. Crocker, D. G. Grier, *J. Colloid Interface Sci.* **179**, 298 (1996).
20. G. Bosma is acknowledged for particle synthesis. This work is part of the research program of the Stichting voor Fundamenteel Onderzoek der Materie (FOM), which is financially supported by the Nederlandse Organisatie voor Wetenschappelijk Onderzoek (NWO). Support through the Transregio Sonderforschungsbereich 6 (SFB-TR6) through the Deutsche Forschungsgemeinschaft (DFG) is acknowledged.

Supporting Online Material
www.sciencemag.org/cgi/content/full/309/5738/1231/DC1
SOM Text
Figs. S1 to S3

5 April 2005; accepted 20 July 2005
10.1126/science.1113207

Osmium Isotope Evidence for an *s*-Process Carrier in Primitive Chondrites

A. D. Brandon,[1]*† M. Humayun,[2]† I. S. Puchtel,[3] I. Leya,[4] M. Zolensky[5]

Osmium extracted from unequilibrated bulk chondrites has isotope anomalies consistent with an insoluble *s*-process carrier, termed Os(i) here. Osmium from metamorphosed bulk chondrites does not have isotope anomalies, implying that the Os(i) carrier was destroyed by metamorphism. The isotopic homogeneity of metamorphosed bulk chondrites is consistent with extremely effective mixing of presolar grains from varied sources in the nebula. Osmium in the Os(i) carrier is likely from nucleosynthetic sites with a neutron density about two to four times as high as that of the average solar *s*-process Os.

Presolar grains (such as SiC and nanodiamonds) are prevalent in unequilibrated chondrites and preserve material from nucleosynthetic processes occurring in the stars from which these grains formed (*1*, *2*). The degree to which these grains and solar material were mixed in the solar nebula is uncertain but important for discerning solar system processes. Isotopic anomalies have been identified in presolar grains and Ca-Al–rich inclusions (CAIs) in chondrites (*1*–*4*). We measured Os isotopes to assess heterogeneities in bulk chondrite meteorites: ^{184}Os is produced by the *p* process only; ^{186}Os [*p*-process contribution 1.1% relative (*5*)] and ^{187}Os are produced by the *s* process and radiogenic decay from